In-situ interferometry study of ionic mass transfer phenomenon during the electrodeposition and dissolution of Li metal in solvate ionic liquids

SCHOLARONE™
Manuscripts

In-situ interferometry study of ionic mass transfer phenomenon during the electrodeposition and dissolution of Li metal in solvate ionic liquids

Akinori Miki, [a] Kei Nishikawa, *[b] Go Kamesui, [a] Hisayoshi Matsushima, [a] Mkito Ueda, [a] and Michel Rosso, [c]

A digital holographic microscope was used to observe the Li+ concentration profile in-situ, accompanied by the electrodeposition and electrochemical dissolution of Li metal in a solvate ionic liquid. The concentration profile showed a linear relationship with the square root of time in a quasi-two-dimensional electrochemical cell that could restrict natural convection fluid motion. For the anodic reaction, the electrochemical dissolution of Li metal induced an increase in concentration in the vicinity of the anode surface. Solvate ionic liquids have an enormous Li salt concentration, and the concentration increase induces a drastic increase in the viscosity of the electrolyte, resulting in a change in cell voltage. In-situ Raman spectroscopy supported the development of the concentration profile near the electrode surface. The coordination of the chemical species also changed with the development of concentration profile induced by electrodeposition and electrochemical dissolution of Li metal in the solvate ionic liquid. This study emphasizes that the development of a concentration profile is more important for a concentrated electrolyte (e.g., solvated ionic liquid) than a conventional 1M class battery electrolyte. This is because the concentration in the vicinity of the electrode can deviate from the ideal molar ratio of Li salt and solvents due to the electrochemical reaction.

Introduction

Lithium-ion batteries (LIBs) are successful energy storage technologies that have significantly changed people's lives. In recent years, the growing demand for high energy density and safety has encouraged researchers to develop electrode materials of advanced LIBs in automobile, stationary electric storage, and aerospace applications. Several studies have focused on the electrolytes, which enable LIBs to be used in diverse applications. Current LIBs use organic solvents and Li salts as electrolytes.[1,2] However, they suffer from low Li+ concentration, flammability, volatility, and concentration polarization during charge and discharge. To fabricate innovative electrolytes, highly concentrated nonaqueous solutions have attracted considerable attention because of their superior characteristics.[3-5] From the 2010s, Watanabe and co-workers reported that the many physicochemical features of specific Li salt and glyme equimolar complexes are similar to ionic liquids.[6-10] Glymes, such as triglyme (G3) and tetraglyme (G4), form one-to-one complexes with certain Li salts. Thus, solvents, such as G3 and

G4, function as ligands for Li+. They made up a new class of electrolytes called "solvate ionic liquids".[11] The Li-solvated ionic liquids exhibit desirable properties as a Li+-conducting electrolyte, including high oxidative stability and high career density as well as ionic-liquid properties, such as high thermal stability and low vapor pressure.[8,12] Therefore, glyme and Li salt equimolar complexes are innovative electrolytes for 4V class LIBs.

Li metal is theoretically the best anode for next-generation Li batteries because it is the lightest metal and has substantial electric capacity.[2,13-15] However, Li-dendrite growth that accompanies the reduction of Li+ is a crucial problem because it degrades the safety and cycling performance.[16-18] In general, metal electrodeposition and dissolution are influenced by the ionic mass transfer properties.[19-23] An electrochemical reaction causes a concentration gradient in the electrolyte from the initial homogeneous distribution. The depletion of deposited ionic species at the electrode surface induces dendrite-shape deposits.[24] The elucidation of an ionic mass transfer phenomenon plays a crucial role in understanding the electrochemical reaction mechanism. Nevertheless, only a few studies have focused on the Li+ concentration profile in Li metal electrodeposition and dissolution.[19,25-28]

In-situ measurements are indispensable for understanding the evolution of the concentration profile in the vicinity of the electrode.[25,29] Several methods can be used to measure the ionic concentration in an electrolyte, e.g., scanning electrochemical

a. Faculty of Engineering, Hokkaido University,Kita 13 Nishi 8, Sapporo, Hokkaido 060-8628, Japan

b. Rechargeable Battery Materials Group, National Institute for Materials Science,1-1 Namiki, Tsukuba, Ibaraki 305-0044, Japan

c. Laboratoire de Physique de la Matière Condensée, École Polytechnique, CNRS, IP-Paris, 91128 Palaiseau cedex, France

microscopy. This technique uses a microelectrode to measure the surface concentration near the electrode interface.[30,31] However, the scanning probe itself might disturb the ion distribution or cause attenuated convection.

Holographic interferometry techniques are alternative noncontact methods.[24,26,29,32,33] The interferometry measurement can visualize a refractive index phase shift corresponding to the concentration profile in real-time from the initial state of the electrolyte solution. The laser beam power is so low that the samples are relatively unaffected during the experiment. Therefore, a digital holographic interferometric microscope (DHM) was used in this study to measure the concentration profile of Li^+. Micro-Raman spectroscopy was also used to investigate the Li^+ concentration and solvation structure near the electrode surface. This should support the results of the interferometry measurement. The peak intensity of typical Raman spectra, which is specific to the coordination in the electrolyte, is proportional to the concentration.[34,35] The final goal of this research is revealing the coupling phenomenon between the ionic mass transfer of Li^+ ion and morphological variation of Li metal electrode. It is indispensable for understanding the interfacial phenomenon to find the transient of coordination of the electrolyte in the vicinity of the electrode. The morphology of electrodeposited Li was also observed by the electron microscope. Here, the transitions of the Li^+ concentration profile, solvation structure, and morphology of the electrodeposited Li metal were examined using LiTFSA (TFSA$^-$ = bis (trifluoromethylsulfonyl) amide) and G4 as the Li salt and solvent, respectively.

Materials and methods

Fig. S1a shows the experimental setup for Li electrodeposition. The cathode was a copper plate (99.99%, Nilaco Co.), and the anode was a Li plate (99.9%, Honjo Metal Co., Ltd.), each 200 μm thick. Fig. S1b shows the experimental setup for Li dissolution. Both electrodes were 200 μm thick Li plates. The Li electrodes were attached to 5 μm thick Cu current collectors that were connected to a potentiostat (SP-150, Bio-logic). The copper electrodes were polished with emery paper (#800 → #1200 → #3000). Before assembling the cell, the surface oxidized layer was removed using 0.1 M HNO_3 aqueous solution and then rinsed with acetone, ethanol, and distilled water.

The electrodes were placed facing parallel to each other in a quasi-two-dimensional cell configuration to minimize the effects of natural convection. A cross-section of the metal plate was used as the working electrode. The surface area of the working electrode was 0.2 mm × 15 mm. The 0.2 mm dimension represents the optical path length for a holographic interferometry microscope.

The electrolyte was prepared from LiTFSA (99.9%, Kishida Chemical Co., Ltd.) and G4 (98%, Kishida Chemical Co., Ltd.). The electrolyte concentration was set from 0.6:1 to 1.5:1 as the molar ratio of LiTFSA and G4. The electrochemical cell and the electrolyte were fabricated in a dry room, where the dew point was under -50℃.

The refractive index of the electrolyte was measured using a digital refractometer (RX-7000α, ATAGO), and the viscosity and density were examined using a rolling-ball viscometer (Lovis 2000ME, Anton Paar). All electrochemical experiment was conducted using LiTFSA and G4 at a 1:1 molar ratio electrolyte in constant current mode (3 mA cm^{-2}) and was controlled using a potentiostat at room temperature.

A DHM (LynceeTec) was used for the in situ measurements of the concentration profile during Li electrodeposition and dissolution. The wavelength of the laser was 683.6 nm. The electrochemical cell shown in Fig. S1 was set to the microscope stage, and the magnification of the objective lens was 5×. The recorded holograms represent the phase change. The holograms were analyzed using Koala software (LynceeTec) to obtain the concentration profile from the concentration dependence of the refractive index. The relationships are described as follows:

$$\Delta n = (\partial n / \partial C) \, \Delta C \qquad (1)$$

$$d\Delta n = (\Delta\theta / 2\pi) \, \lambda \qquad (2)$$

where Δn is the change in refractive index, ΔC is the change in Li^+ ion concentration, d represents the optical path length (0.2 mm, here), $\Delta\theta$ describes phase change of refractive index, and λ denotes the wavelength of the laser. The Li^+ ion concentration profile was calculated from the phase change based on these relationships.

Quasi-two-dimensional electrochemical cells were also used in the optical absorption experiment. The Cu working electrode was 0.1mm thick. Li metal was placed at the anode surface in a glove box filled with purified Ar. The cell was closed tightly by two silicone rubber gaskets pressed on both sides by a mechanical piston to seal the electrolyte. The electrodes were set in the vertical direction, with the cathode on the top and the anode at the bottom, to restrict the natural convection induced by the electrolysis. The light sources consisted of a battery of 16 light-emitting diodes (LEDs) with a wavelength of 770 nm or a single LED with a wavelength of 365 nm. The black and white images were pictured at one-second intervals. The recorded data were analyzed using the ImageJ program.

Raman spectra of the electrolytes were measured at room temperature using a laser micro-Raman spectrometer (LabRAM1B, HORIBA), which was calibrated using a Si single crystal before the measurements. The wavelength of the excitation laser was 632.7 nm. The apparatus resolution was approximately 1 cm^{-1}. The exposure time and cumulative numbers were five seconds and five times for the in-situ measurements and 10 seconds and five times for the reference data of each electrolyte, respectively. The Raman spectra were deconvoluted with the software of GRAMS-AI (Thermo Fisher Scientific K. K.) to extract the single Raman bands.

The electrodeposited Li was observed by scanning electron microscopy (SEM, JSM-7800F, JEOL) and transmission electron microscopy (TEM, JEM-ARM200F, JEOL). The working electrodes with the electrodeposited Li were rinsed carefully with G4 and DME (G1) and placed in an air-tight holder to prevent air exposure for transfer to SEM or TEM.
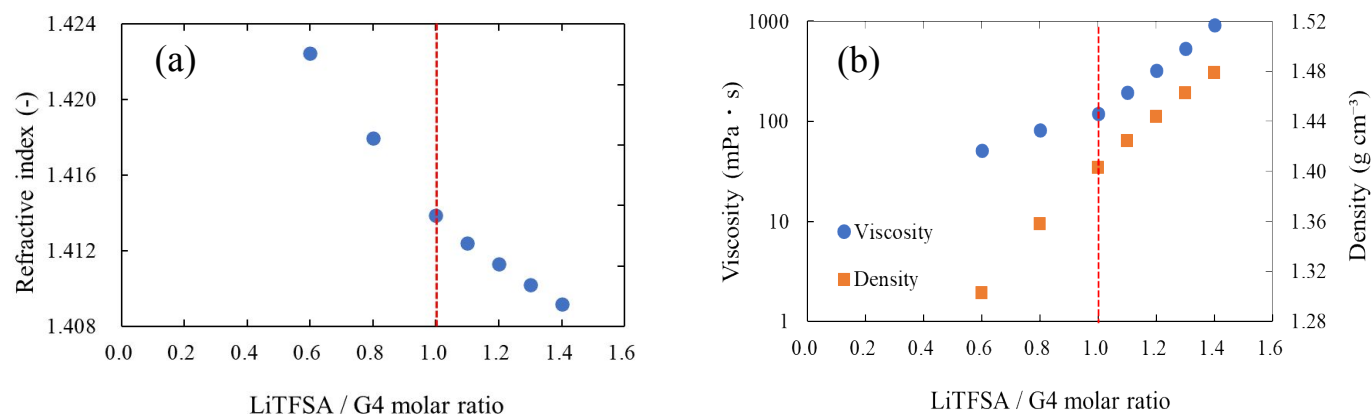
Fig. 1 Refractive index (a) density and viscosity (b) of the LiTFSA and G4 mixtures at room temperature.

STEM-EELS analyzed the chemical species. TEM and STEM-EELS were conducted at -160℃ using a cryo-TEM holder.

Results and Discussion

Property of electrolytes

Fig. 1a shows the concentration dependence of the refractive index of LiTFSA and G4 mixtures at room temperature. The LiTFSA to G4 molar ratio represents the electrolyte concentration. The refractive index decreased with increasing concentration. This decrease rate was smaller when the concentration was increased above a 1:1 LiTFSA:G4 molar ratio. Accordingly, different constants of proportionality between the refractive index and the concentration were used to calculate the concentration profile during the electrodeposition and dissolution of Li.

Fig. 1b shows the density and viscosity of LiTFSA and G4 mixtures at room temperature. The density was almost proportional to the concentration, but the rate of increase became slower above a 1:1 molar ratio. The viscosity as a function of concentration is shown in a logarithmic plot. The increase in viscosity accelerated above a 1:1 molar ratio. From these results, the physicochemical properties of the LiTFSA and G4 mixtures appeared to change at a 1:1 molar ratio as a border. The conductivity is approximately proportional to reciprocal viscosity, suggesting that the mobility of the ions in the solvate ionic liquids is determined mainly by the fluidity of the media.[36] In the present system, the viscosity increased with increasing molar ratio of the electrolyte. The conductivity of the electrolyte decreased significantly as the concentration increased.

Cathode part

Cu and Li were used as the working and counter electrodes, respectively, for in-situ observations of the concentration profile during Li electrodeposition, as shown in Fig. S1. The DHM movie (10x speed) for the electrodeposition of Li metal is ESI movie S1. The left side is electrode and the blue area is electrolyte. After the electrodeposition started, the color was

changing in the electrolyte. The color change means the change of refractive index of the electrolyte corresponding to $\Delta\theta$ in Eq. (2).

Fig. 2a shows the concentration profile of the electrolyte in the vicinity of the cathode during Li electrodeposition. The concentration profile from the electrode surface to the bulk of the electrolyte was visualized successfully. Transient behavior was recorded; the surface concentration decreased, and the diffusion layer grew with time. The authors previously reported in-situ measurements of the Cu^{2+} ion concentration near the cathode in the magnetic field during Cu electrodeposition.[24] In that study, the electrolyte was an aqueous solution, and the diffusion layer thickness grew to more than 600 μm within 100 s after applying the current. However, diffusion layer thickness grew only 70 μm at 100 s after Li electrodeposition started in this measurement. The growth rate of the diffusion layer thickness was slower than that of the aqueous solution. This was attributed to the difference in diffusion coefficient. At approximately 210 s, the electrode surface moved towards the electrolyte because Li metal was electrodeposited on the electrode surface. Here, 0 μm of the horizontal axis was defined as the cathode surface before the experiment started.

Fig. 2b shows the LiTFSA to G4 molar ratio at the cathode surface and the cell voltage as a function of the square root of time. The cell voltage became lower than 0 V several seconds after the current was applied. Only a slight change in surface concentration was observed because the applied current was consumed by reducing the surface oxide film on the Cu electrode. At 4 s, the cell voltage became negative, and the surface concentration began to decrease. The cell voltage decreased continuously to reach a constant value. In this initial region, the electrodeposition of Li metal and the reduction of the oxide film were carried out. The surface oxidation of the Cu working electrode was unavoidable when the electrochemical cell was assembled, even though the Cu oxide film was removed before assembling. The surface concentration decreased with increasing square root of time. After 100 s, the decrease in surface concentration became moderate. One of the reasons was that the Li metal irregular dendrites became an obstacle to define the exact electrode surface. Another reason was that natural
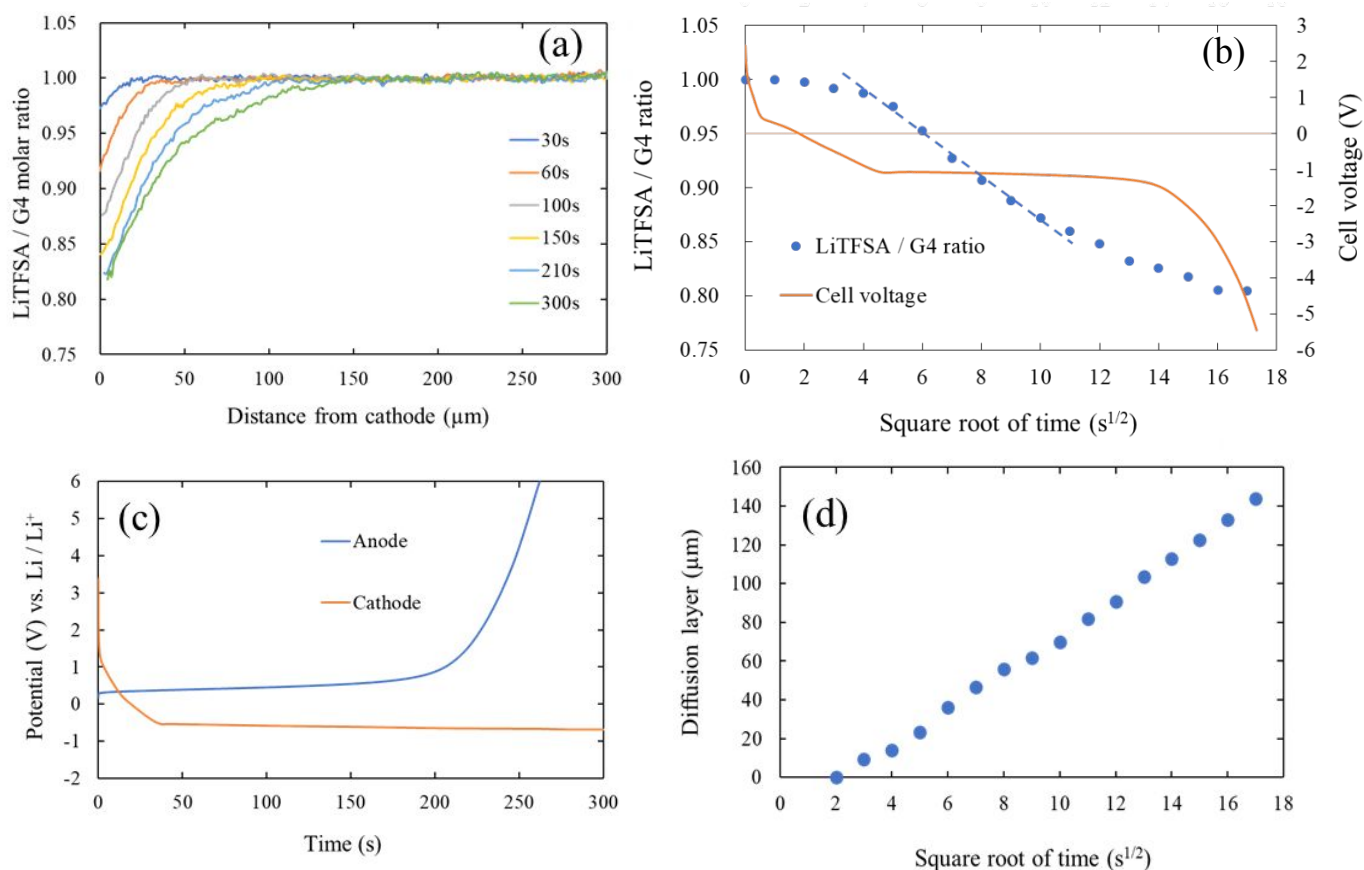
Fig. 2 (a) Concentration profile of the electrolyte in the vicinity of the cathode during Li electrodeposition. (b) Molar ratio of LiTFSA and G4 at the cathode surface and cell voltage as a function of the square root of time. (c) Anodic and cathodic potential of time using Li foil as a reference electrode. (d) Diffusion layer thickness as a function of the square root of time.

convection was induced by the decrease in electrolyte density near the cathode, accompanied by the consumption of Li$^+$ at the cathode surface. Natural convection stirred the electrolyte and attenuated the decrease in concentration. After 190 s, the cell voltage decreased drastically. Another experiment was conducted by introducing a reference electrode to determine which electrode contributed to this phenomenon.

Fig. 2c shows the time transient of the anodic and cathodic potential against the Li metal reference electrode. The cathodic potential decreased immediately after the current had been applied. The anodic potential remained almost constant. At this stage, the cell voltage depended on the cathodic potential, as shown in Fig. 2b. After 190 s, the anodic potential increased sharply. Therefore, the drastic divergence of the cell voltage was caused by the anodic potential, as shown in Fig 2b.

Fig. 2d shows the development of the diffusion layer thickness as a function of the square root of time obtained from the concentration profile. The diffusion layer thickness did not grow during the initial 4 s. This agrees with the surface concentration change shown in Fig. 2b. As mentioned above, the reduction of the Cu oxide layer occurred in this very initial stage. As the electrodeposition of Li metal started, the diffusion layer thickness grew proportionally with the square root of time. Here, the diffusion coefficient of Li$^+$ was estimated from the following

equation introduced by the Nernst-Planck equation and Fick's laws of diffusion.

$$\delta = \sqrt{(4Dt/\pi)} \qquad (3)$$

where δ is the diffusion layer thickness, D is diffusion coefficient, and t is time. The diffusion coefficient of Li$^+$ was 6.4×10^{-7} cm^2 s^{-1}. This calculation was conducted based on the region in proportion to the square root of time for the initial 100 s because natural convection will affect the development of the concentration profile after 100 s. An in-situ optical absorption experiment was also conducted using the cathode over anode (C/A) configuration to suppress the influence of natural convection. The diffusion layer thickness can grow without the influence of natural convection because the cathode plane was facing downward horizontally. Fig. S2 shows that the diffusion layer thickness grew with increasing square root of time after an incubation time of 4 s. This agrees with Fig. 2d. However, the estimated diffusion coefficient from this measurement was 3.7×10^{-7} cm^2 s^{-1}, which was relatively smaller than that obtained from the interferometry experiment shown in Fig.2. This difference might be caused by the influence of natural convection in interferometry experiments. A way to prevent natural convection would be to conduct the experiment in zero-gravity.[37, 38] Continuous attempts will be made to eliminate the

effects of natural convection by making the thickness of the electrochemical cell thinner.

In-situ Raman spectroscopy was utilized to examine the result of digital holographic interferometry measurement. First, we measured the reference Raman spectra of the electrolyte with various concentrations. Fig. 3a presents Raman spectra of LiTFSA powder, pure G4, and various electrolytes composed of LiTFSA and G4, in the range from 720 to 760 cm^{-1}. The TFSA$^-$ anion has a strong band at 740–750 cm^{-1}, which has been assigned to the coupled motions of CF$_3$ bending and S–N stretching.[39] This band is susceptible to interactions with Li$^+$. The band corresponding to solvent-separated ion pairs (SSIPs) or an uncoordinated TFSA$^-$ anion appeared around 739–742 cm^{-1}, whereas the band appearing around 745–755 cm^{-1} originates from TFSA$^-$ bound directly to Li$^+$ in the form of contact ion pairs (CIPs) or more than two Li$^+$ ions in the form of aggregates (AGGs).[40] The peak around 741 cm^{-1} increased with increasing LiTFSA concentration until an equimolar electrolyte of LiTFSA and G4 was achieved. However, the peak decreased, and another peak around 747 cm^{-1} increased when the LiTFSA concentration

became higher than equimolar. CIPs and AGGs increased when the LiTFSA concentration became higher than equimolar. The increase in such aggregates will increase the viscosity of the electrolyte. In addition, the LiTFSA powder had a peak at around 747 cm^{-1}, showing that this peak corresponds to TFSA$^-$ bound directly to Li$^+$.

Fig. 3b presents the Raman spectra of the same materials for Fig. 3a, ranging from 800 to 900 cm^{-1}. For glymes, the Raman bands between 800 and 900 cm^{-1} were assigned to the coupled modes of the rocking vibration of the CH$_2$ groups and the stretching vibration of C–O groups.[41] Pure G4 has three strong bands at 809, 828, and 851cm^{-1}, with no visible bands in the range, 865–890 cm^{-1}.[10] The free G4 molecule decreased with increasing LiTFSA concentration. On the other hand, an intense peak appeared at approximately 870 cm^{-1} for a mixture of LiTFSA and G4. This was attributed to complex formation with metal ions called the breathing mode.[41] The peak intensity showed a maximum at a 1:1 equimolar electrolyte because a 1:1 equimolar electrolyte forms a solvation structure. The peak at approximately 870 cm^{-1} decreased when there was more LiTFSA
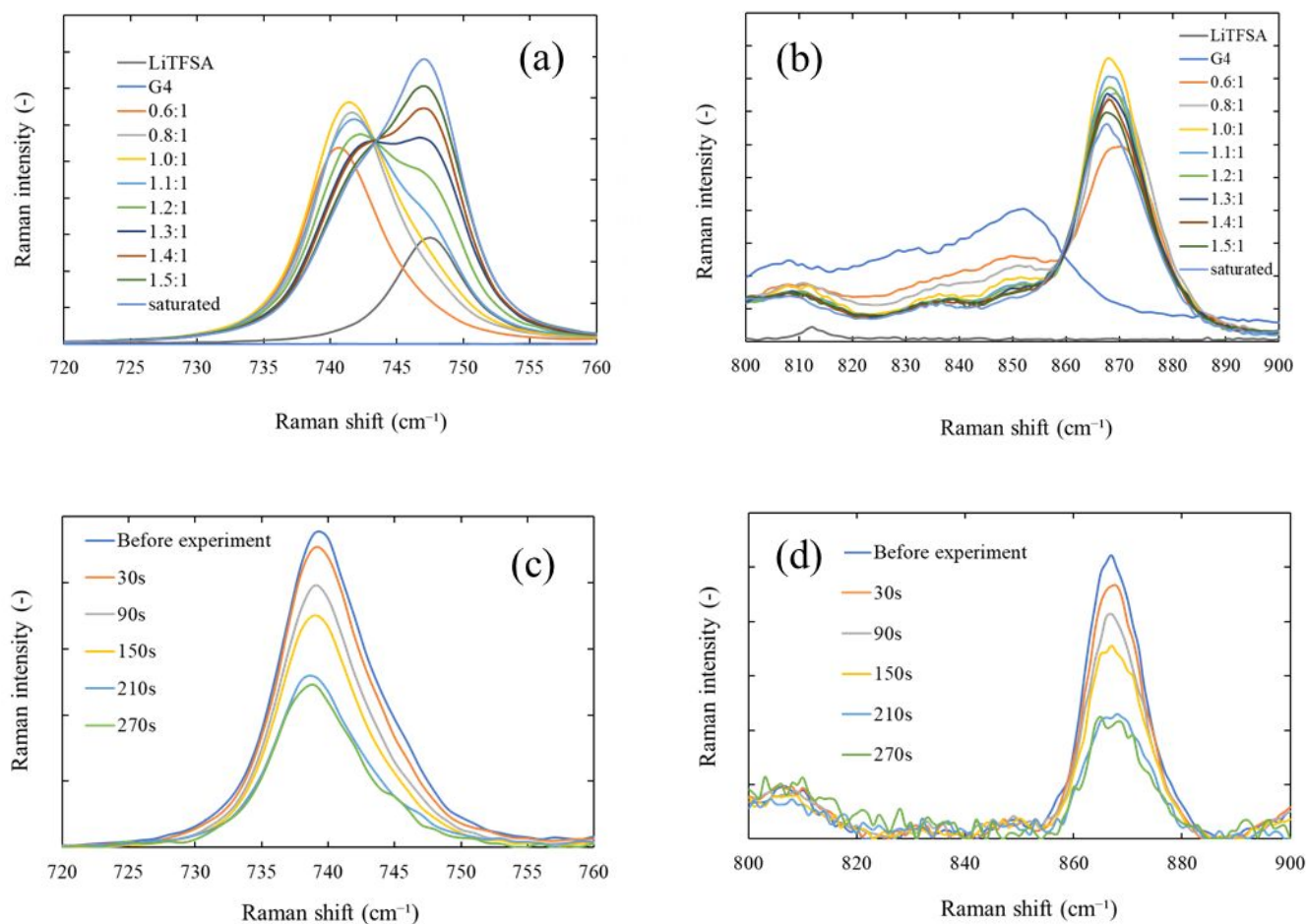

Fig. 3 Raman spectra of LiTFSA powder, pure G4 and various electrolytes composed of LiTFSA and G4, in the range from 720 to 760 cm^{-1} (a), in the range from 800 to 900 cm^{-1} (b). In-situ Raman spectra of the electrolyte in the vicinity of cathode surface during Li electrodeposition, in the range from 720 to 760 cm^{-1} (c), in the rangef from 800 to 900 cm^{-1} (d).

than G4, which was related to CIP formation. From the viewpoint of the interaction of glymes, the HOMO (Highest Occupied Molecular Orbital) energy levels of glymes in the cation-glyme-TFSA- complexes were higher than those of the cation-glyme complexes.[42] This is affected by the interaction of cations, anions, and solvent. Hence, excessive LiTFSA might influence the bonding of a complex composed of Li+ and G4.

Fig. 3c shows the Raman spectra of the electrolyte in the vicinity of the cathode surface during Li electrodeposition, ranging from 720 to 760 cm^{-1}. The peak at approximately 741 cm^{-1} showed the highest intensity before electrodeposition and decreased after the current was applied. This result suggests that TFSA- was decreasing to maintain electrical neutrality as the Li+ concentration decreased by the electrodeposition. G4 desorbed from the solvation structure might compensate for the uneven distribution of electric charge by coordinating to TFSA-. However, the coordination change did not influence the electric conduction mechanism because the cathodic potential was constant. The peak at 741 cm^{-1} shifted slightly and transition of the peak shoulder was asymmetry as progress of the electrodeposition. Therefore, the peak at approximately 747 cm^{-1} also decreased with the progress of Li electrodeposition. This suggests that TFSA- bound directly to Li+ exists even when the concentration is equimolar. According to the literature, the preferred coordination number of Li+ in solution is 4 or 5.[43] Five ether oxygen atoms were considered to coordinate to Li+ in the structure of the [Li(G4)]+ complex cation, but SSIPs and CIPs were found. Aguilera et al. also revealed CIPs in an equimolar mixture of LiTFSA and G4.[44]

Fig. 3d shows the in-situ Raman spectra of the same measurement for Fig. 3c, ranging from 800 to 900 cm^{-1}. The peak at approximately 870 cm^{-1} showed the highest intensity before electrodeposition and decreased as electrodeposition proceeded because G4 was desolvated by the Li+ ion.[45] These transient behavior agreed with the results of the interferometry measurement. However, three specific peaks for free G4 did not appear in this measurement. There are two possible causes. The first is that the Raman spectra in this in-situ measurement had a larger background than the reference measurements shown in

Fig.3a and b. because the accumulation time is half of the reference measurements. In addition, it was difficult to recognize the transition of the Raman spectra because the peaks of this range were originally weaker than those ranging from 720 to 760 cm^{-1} and around 870 cm^{-1}. Moreover, there was only a tiny difference in the peak for free G4 between LiTFSA to G4 molar ratio of 1:1 (yellow line) and 0.8:1 (grey line), as shown in Fig. 3b. The electrodeposited Li would also react with G4 desolvated from Li+ to form solid electrolyte interphase (SEI) layer. The solvent was reported to decompose, and SEI formed on the electrodeposited Li.[46-48] The composition of SEI depends on the Li salt and solvent. In addition, it was reported that SEI affects the morphology of the subsequent electrodeposited Li.[46-48] In this experiment, distinct peaks for free G4 may not have been observed because G4 decomposed concomitantly with Li electrodeposition.

Fig. 4 shows an SEM image and a cryo-TEM image of the cathode after Li electrodeposition. The electrodeposited Li was composed of columnar and angular blocks with needle-shaped dendrites. The electrode surface morphology became considerably rough as Li electrodeposition progressed. As described above, such dendrite growth prevented to define the precise electrode surface in the digital holographic interferometer microscope images. In this study, Li+ was not depleted at the cathode surface, as shown in Fig. 2b. Therefore, the rough morphology of the cathode surface was not caused by the depletion of reactants in the vicinity of the electrode. In previous research with the same electrochemical cell but different electrolytes, more whisker-like dendrites could be observed, which might have been influenced by the solvent, anions, and Li+ concentration.[26, 27] These differences in chemical species in the electrolyte induced the different composition of SEI formed on the electrodeposited Li. Accordingly, the surface of electrodeposited Li was analyzed using a cryo-STEM-EELS technique.[49] The Cryo-TEM technique can reveal the nature of the Li metal electrode surface because Li metal is vulnerable to electron beams. Electrodeposited Li from a 1:1 equimolar electrolyte of LiTFSA and G4 in this experiment was still damaged and deformed by the electron beam even in the cooling
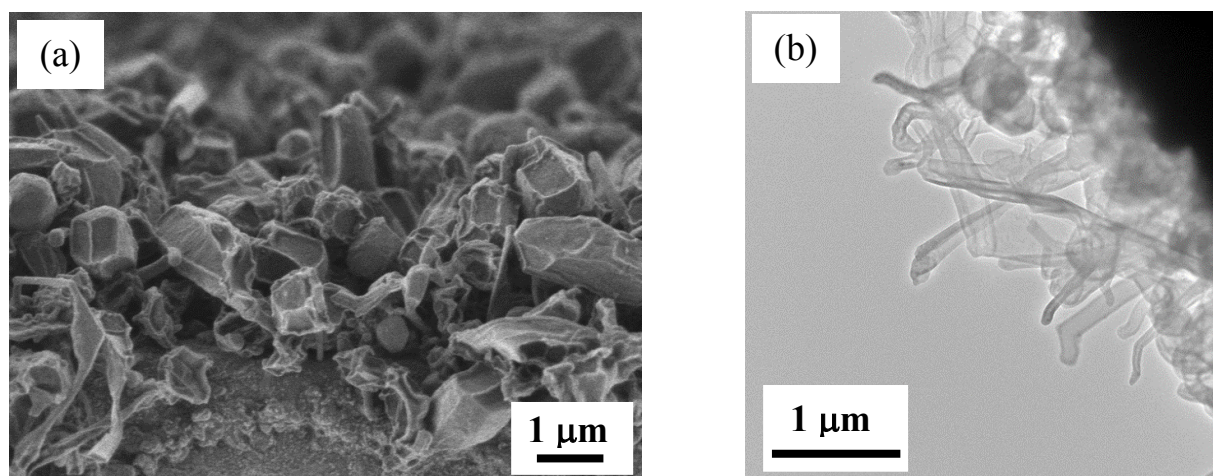

Fig. 4   SEM image (a) and STEM image (b) of the cathode electrode after Li electrodeposition.

environment. Therefore, it was difficult to observe a distinct lattice image with high magnification. However, STEM-EELS could be conducted by reducing the emission current and defocus method. Fig. S4 presents a STEM image and mapping images based on the EELS spectra. The authors already acquired the EELS spectra of various Li compounds under the cooling environment in the same experimental procedure.[49] The database was used for this analysis. From the obtained spectra, SEI was composed mainly of Li_2O and a small amount of LiOH as shown in the mapping images of Fig. S4. Decomposition of the solvent or anions might progress with Li electrodeposition to form the SEI layer because the solvent and anions contain oxygen atoms. The previous research demonstrated the formed SEI onto the electrodeposited Li metal in 1M LiTFSA-G4 electrolyte was mainly composed of Li_2O.[49] The LiOH formation is typical feature of SEI composition in the solvate ionic liquid electrolyte system. For a detailed discussion of the SEI formation mechanism, a new study should be designed by changing the concentration and component of the electrolyte and other techniques.

Anode part

Li foil was used as both the working and counter electrodes for the electrochemical dissolution of Li. The DHM movie (10x speed) for the electrochemical dissolution of Li metal is ESI movie S2.

Fig. 5a shows the evolution of the concentration profile in the electrolyte near the anode during electrochemical dissolution. As soon as the current was applied, the Li^+ surface concentration increased, and the diffusion layer grew. The variation of the Li^+ concentration at the anode surface was larger than that near the cathode. This is because the diffusion coefficient of Li^+ decreased with increasing concentration near the anode by the electrochemical dissolution of Li, as shown in Fig. 2a. In addition, the increase in concentration induced an increase in the viscosity of the electrolyte, suggesting that the effect of natural convection was much smaller at the anodic side than at the cathodic side.[36]

Fig. 5b shows the transition of the LiTFSA to G4 molar ratio at the anode surface and the cell voltage as a function of the square root of time. The surface concentration of Li^+ increased with increasing square root of time. The cell voltage first showed a constant value after the electrochemical dissolution started. At 130 s, the cell voltage increased drastically because a decrease in conductivity was induced near the anode surface. This was attributed to a continuous increase in viscosity due to an increase in surface concentration. Consequently, the electrochemical dissolution of Li metal was inhibited. At 180 s, the increase in cell voltage slowed down. At the same time, the increase in surface concentration became slightly moderate. Unexpected reactions, such as oxidation decomposition except for Li electrochemical dissolution, might have been induced.[8] The
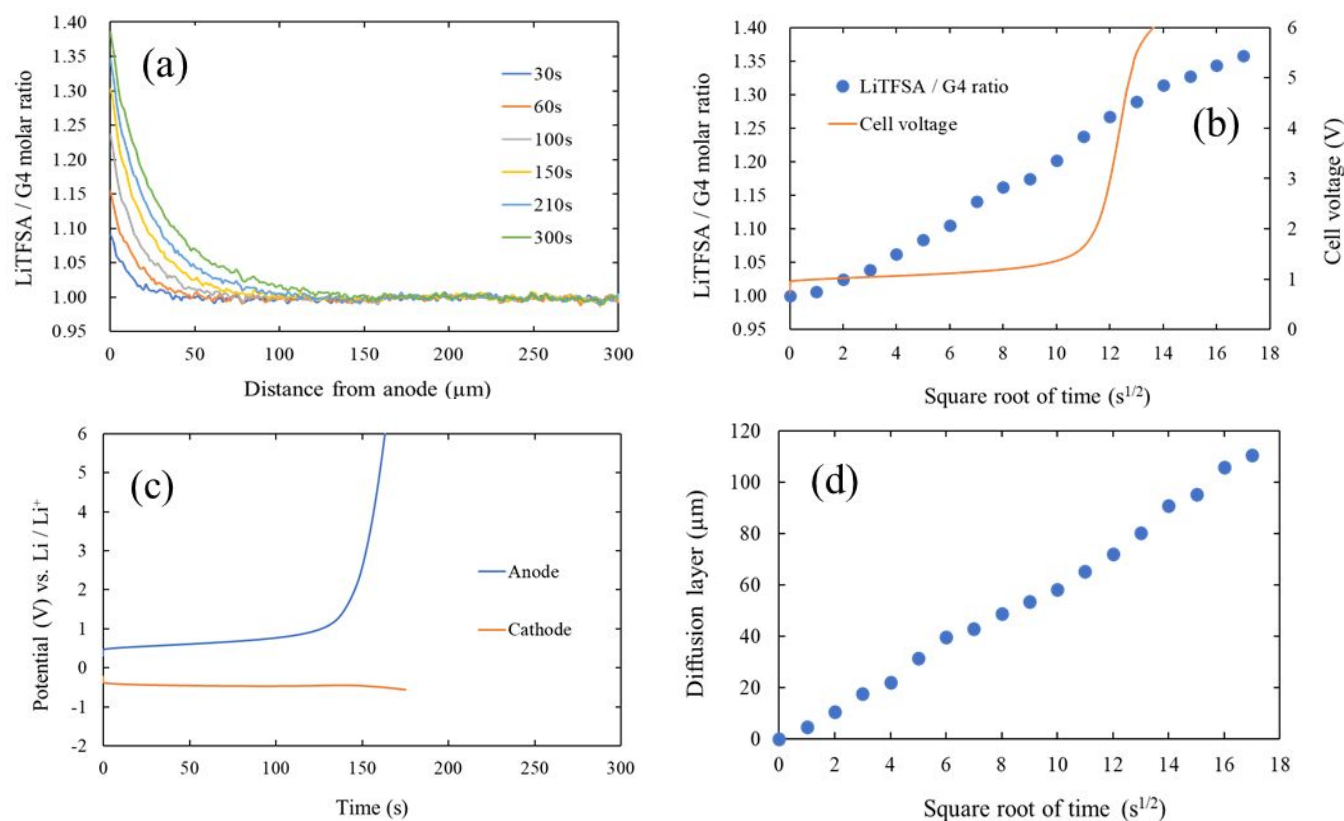

Fig. 5 (a) Concentration profile of the electrolyte in the vicinity of anode during Li dissolution. (b) Molar ratio of LiTFSA and G4 at the anode surface and cell voltage as a function of the square root of time. (c) Anodic and cathodic potential of time using Li foil as the reference electrode. (d) Diffusion layer thickness as a function of the square root of time.

potential behavior of both electrodes was investigated by introducing a Li metal reference electrode. Fig. 5c shows the time evolution of the anodic and cathodic potentials. Both the anodic and cathodic potentials showed constant value after electrolysis started because both electrodes were Li metal. At 130 s, the anodic potential increased sharply, coinciding with the cell voltage profile shown in Fig.5b. The cathodic potential showed an almost constant potential, whereas the anodic potential increased. Therefore, the increase in cell voltage shown in Fig. 5b was caused by the increase in anodic potential. This behavior is consistent with the discussion in the cathodic part shown in Fig.2.

Fig. 5d shows the development of the diffusion layer thickness as a function of the square root of time. The development of the diffusion layer thickness was proportional to the square root of time immediately after the current was applied. The diffusion coefficient of Li^+ was estimated to be 2.9×10^{-7} $cm^2 \, s^{-1}$ within 100 s after electrolysis had started. The diffusion coefficient based on electrochemical dissolution was smaller than that from Fig.2d in the case of electrodeposition. However, it almost agreed with that obtained from Fig. S2 in the optical absorbance experiment with the C/A configuration. The influence of natural convection was less on the anodic side than the cathodic side because the viscosity of the electrolyte increased with increasing Li^+ concentration. Therefore, an almost ideal measurement could be realized in terms of the restriction of natural convection in the early stages of electrochemical dissolution.

As well as the discussion in cathode part, in-situ Raman spectroscopy measurement was conducted to examine the validity of the results of interferometry measurement. Figure. 6a shows the time transient Raman spectra of the electrolyte near the anode surface during Li electrochemical dissolution, ranging from 720 to 760 cm^{-1}. The peak at approximately 741 cm^{-1} had the highest intensity before electrochemical dissolution. The peak decreased, and that at approximately 747 cm^{-1} increased as the electrochemical reaction proceeded. This suggests that the amount of $TFSA^-$ bound directly to Li^+ increased due to the increase in Li^+ concentration accompanied by the electrochemical dissolution of Li metal.[40] Peak intensity analysis

of the Raman spectra was conducted to examine the interferometry measurement. The Raman spectra were deconvoluted into two bands at around 741 and 747 cm^{-1} using two Gaussian functions. Fig. S3 shows the ratio of the integrated intensity originating from 741 and 747 cm^{-1} in the electrolyte at each concentration shown in Fig. 3a. The concentration was estimated based on the Raman spectra shown in Fig.6a using this relationship between the peak intensity ratio and the molar ratio of the electrolyte. Fig.S5 compares the measured surface concentration from interferometry and that from Raman spectroscopy during the electrochemical dissolution of Li. The red plots indicate the intermediate time of the measurement and the error bars of the red plots are related to the measuring time of 25 s. In the interferometry technique, concentration change could be measured with high accuracy because the resolution was approximately 1 μm. Therefore, it could be measured simultaneously at approximately 1 μm intervals from the electrode to the bulk of the electrolyte. In the Raman spectra, the concentration change was measured at a single point chosen manually near the electrode. Hence, it is possible to measure the concentration closer to the electrode surface in the interferometry technique. This can explain the slight disagreement of the surface concentration between the interferometry measurements and Raman spectroscopy results. Hence the agreement between the results regarding the anode surface concentration obtained from both techniques was satisfactory.

Fig. 6b shows the time transient of the Raman spectra in the same measurement as Fig. 6a, ranging from 800 to 900 cm^{-1}. The peak at approximately 870 cm^{-1} showed the highest intensity before the electrochemical dissolution of Li and decreased slightly after the current was applied. This suggests that the 1:1 balance of LiTFSA and G4 was lost because the Li^+ ion concentration was greater than G4 at the anode surface. The increase in CIPs with the dissolution of Li metal was confirmed, as shown in Fig. 6a. The increased Li^+ ion might form CIPs by sharing G4. Such a shared G4 by Li^+ exists because the CIPs were confirmed even in an equimolar mixture of LiTFSA and G4, as shown in Fig. 3c. However, there was a smaller difference in the peak intensity at approximately 870 cm^{-1} compared to the cathodic data shown in Fig. 3d. Focusing on the peak at 870 cm^{-1}
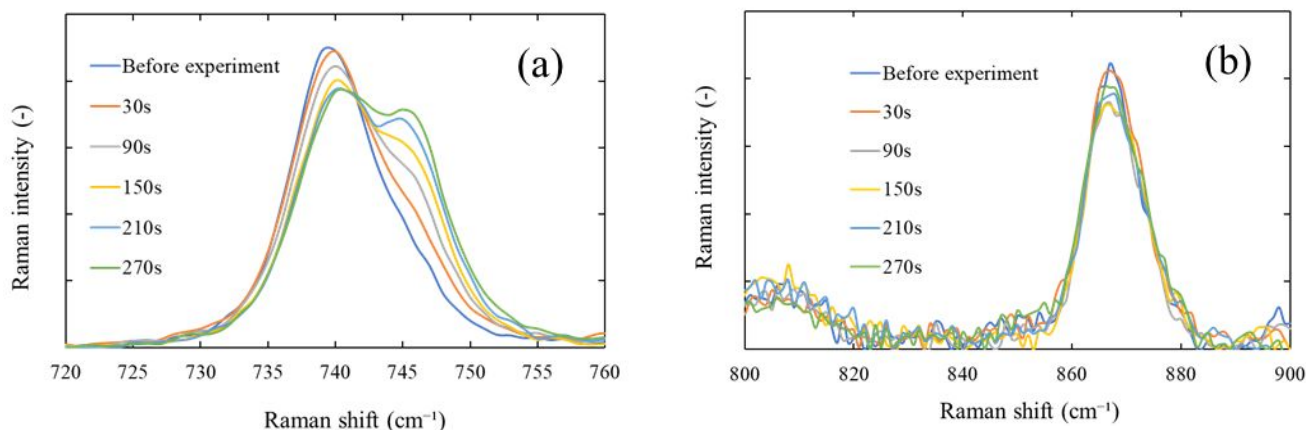

Fig. 6   In-situ Raman spectra of the electrolyte in the vicinity of anode surface during Li dissolution, in the range from 720 to 760 cm^{-1} (a), in the range from 800 to 900 cm^{-1} (b).

Journal Name

ARTICLE

in Fig. 3b as reference data, the variation of the Raman spectra between 1:1 (yellow line) and 1.4:1 (brown line) was smaller than that of between 1:1 and 0.6:1 (orange line). Therefore, the variation of the intensity of this peak in the Raman spectra is difficult to detect during the electrochemical dissolution. This suggests that G4 has little influence on solvation with Li^+, even if CIPs and AGGs are formed, compared to desolvation with Li electrodeposition on the cathodic side. The differences in the interactions of LiTFSA and G4 between the cathode and anode surface are discussed based on these results. At the cathode surface, G4 was desolvated from Li^+ with Li electrodeposition, and the concentration of free G4 molecules increased near the cathode surface. This caused a decrease in viscosity and enhanced fluid motion due to natural convection. In contrast, $TFSA^-$ bound directly to a Li^+ ion in the form of CIPs increased at the anode surface, suggesting that AGGs with $TFSA^-$ bound directly to more than two Li^+ ions were also formed. This contributed to the increase in viscosity. In addition, free G4 decreased with increasing Li^+ concentration at the anode surface from Fig. 3b and Fig. 6b. From these results, a sharp decrease in free G4 might cause an increase in anode potential as the Li^+ ion concentration increases because such G4 might be required to coordinate to the Li^+ ion during Li dissolution.[9]

The application of concentrated electrolytes, such as that solvate ionic liquid used in this study, is promising for the next generation Li batteries. Nevertheless, it is essential to understand the interface phenomenon during the electrodeposition and electrochemical dissolution of Li metal from the viewpoint of ionic mass transfer to develop high-power Li metal batteries. The results obtained in this study appeal the usefulness of the interferometry technique in order to discuss the ionic mass transfer phenomenon during the cycle of Li metal electrode.

Conclusions

Digital holographic interferometry was used to visualize the Li^+ ion concentration profile near the cathode and anode during the electrodeposition and dissolution of Li, respectively. The transient behavior of the electrolyte was measured. At the cathodic side, the Li^+ concentration and viscosity decreased. Hence, natural convection may affect the development of a concentration profile in the long-time range, even in the quasi-two-dimensional electrochemical cell. The diffusion coefficient of Li^+ was estimated to be 6.4×10^{-7} cm² s⁻¹ with the cell, and 3.7×10^{-7} cm² s⁻¹ was using the cathode over anode configuration cell that restricted the natural convection effect. The transient Raman spectra supported the validity of the interferometry measurement, and suggested that G4 was desolvated from the solvation structure due to Li electrodeposition. STEM-EELS showed that Li_2O-rich SEI including LiOH was formed due to electrolyte decomposition on the electrodeposited Li surface from the 1:1 equimolar electrolyte of LiTFSA and G4. At the anodic side, the Li^+ ion concentration and viscosity increased as Li dissolution progressed. The diffusion coefficient of the Li^+ ion was 2.9×10^{-7} cm² s⁻¹, suggesting that the increase in viscosity impeded

the effects of natural convection. Raman spectroscopy showed the concordant behavior with the interferometry results and that CIPs and AGGs were formed near the anode. This behavior is consistent with the increase in electrolyte viscosity. Moreover, a sharp decrease in the free G4 molecule might cause an increase in anode potential because free G4 might be required for Li dissolution.

Author Contributions

A.M. conducted the experiments, analyzed the results, and wrote the article. K. N. designed the research and experiments and edited the article. G.K. helped in the analysis and preparing the schematic diagrams. H. M., M. U., and M. R. supervised the research.

Conflicts of interest

There are no conflicts to declare.

The authors declare no conflicts of interest.

References

1. R. Fong, U. von Sacken and J. R. Dahn, *J. Electrochem. Soc.*, 1990, **137**, 2009.
2. D. Aurbach, A. Zaban, Y. Ein-Eli, I. Weissman, O. Chusid, B. Markovsky, M. Levi, E. Levi, A. Schechter and E. Granot, *J. Power Sources*, 1997, **68**, 91.
3. Y. Yamada, Y. Takazawa, K. Miyazaki and T. Abe, *J. Phys. Chem. C*, 2010, **114**, 11680.
4. Y. Yamada, M. Yaegashi, T. Abe and A. Yamada, *Chemi. Commun.*, 2013, **49**, 11194.
5. Y. Yamada, K. Furukawa, K. Sodeyama, K. Kikuchi, M. Yaegashi, Y. Tateyama, and A. Yamada, *J. Am. Chem. Soc.*, 2014, **136**, 5039.
6. T. Tamura, T. Hachida, K. Yoshida, N. Tachikawa, K. Dokko and M. Watanabe, *J. Power Sources*, 2010, **195**, 6095.
7. K. Yoshida, M. Tsuchida, N. Tachikawa, K. Dokko and M. Watanabe, *J. Phys. Chem. C*, 2011, **115**, 18384.
8. K. Yoshida, M. Nakamura, Y. Kazue, N. Tachikawa, S. Tsuzuki, S. Seki, K. Dokko and M. Watanabe, *J. Am. Chem. Soc.*, 2011, **133**, 13121.
9. K. Ueno, K. Yoshida, M. Tsushida, N. Tachikawa, K. Dokko and M. Watanabe, *J. Phys. Chem. B*, 2012, **116**, 11323.
10. K. Ueno, R. Tatara, S. Tsuzuki, S. Saito, H. Doi, K. Yoshida, T. Mandai, M. Matsugami, Y. Umebayashi, K. Dokko and M. Watanabe, *Phys. Chem. Chem. Phys.*, 2015, **17**, 8248.
11. T. Tamura, K. Yoshida, T. Hachida, M. Tsuchiya, M. Nakamura, Y. Kazue, N. Tachikawa, K. Dokko and M. Watanabe, *Chem. Lett.*, 2010, **39**, 753.

12. D. W. McOwen, D. M. Seo, O. Borodin, J. Vatamanu, P. D. Boyle and W. A. Henderson, *Energy Environ. Sci.*, 2014, **7**, 416.

13. M. Odziemkowski and D. E. Irish, *J. Electrochem. Soc.*, 1992, **139**, 3063.

14. K. Kanamura, H. Takezawa, S. Shiraishi and Z. Takehara, *J. Electrochem. Soc.*, 1997, **144**, 1900.

15. K. Naoi, M. Mori, Y. Naruoka, W. M. Lamanna and R. Atanasoski, *J. Electrochem. Soc.*, 1999, **146**, 462.

16. X. B. Cheng and Q. Zhang, *J. Mater. Chem. A*, 2015, **3**, 7207.

17. K. H. Chen, K. N. Wood, E. Kazyak, W. S. LePage, A. L. Davis, A. J. Sanchez and N. P. Dasgupta, *J. Mater. Chem. A*, 2017, **5**, 11671.

18. F. Wu, Y. X. Yuan, X. B. Cheng, Y. Bai, Y. Li, C. Wu and Q. Zhang, *Energy Storage Materials*, 2018, **15**, 148.

19. K. Nishikawa, Y. Fukunaka, T. Sakka, Y. H. Ogata and J. R. Selman, *J. Electrochem. Soc.*, 2007, **154**, A943.

20. S. Kawai, K. Nishikawa, Y. Fukunaka, and S. Kida, *Electrochim. Acta*, 2007, **53**, 257.

21. M.C. Ribeiro, L.G.C. Rego and P.C.T. D'Ajello, *J.Electroanal. Chem*. 2009, **628**, 21.

22. S. Kawai, K. Nishikawa, Y. Fukunaka, and S. Kida, *Electrochemistry*, 2009, **77**, 601.

23. T. Chang, Y. Jin, L. Wen, C. Zhang, C. Leygraf, I. O. Wallinderb and J. Zhang, *Electrochim. Acta*, 2016, **211**, 245.

24. K. Nishikawa, T. Saito, H. Matsushima and M. Ueda, *Electrochim. Acta*, 2019, **297**, 1104.

25. A. Teyssot, C. Belhomme, R. Bouchet, M. Rosso, S. Lascaud, M. Armand, *J.Electroanal. Chem*. 2005, **584**, 70.

26. K. Nishikawa, T. Mori, T. Nishida, Y. Fukunaka, M. Rosso and T. Homma, *J. Electrochem. Soc.*, 2010, **157**, A1212.

27. K. Nishikawa, T. Mori, T. Nishida, Y. Fukunaka, M. Rosso, *J. Electrochem. Soc.*, 2011, **661**, 84.

28. S. A. Krachkovskiy, J. D. Bazak, P. Werhun, B. J. Balcom, I. C. Halalay and G. R. Goward, *J. Am. Chem. Soc.*, 2016, **138**, 7992.

29. A. Miki, K. Nishikawa, T. Ozawa, H. Matsushima and M. Ueda, *J. Electrochem. Soc.*, 2020, **167**, 062501.

30. J. Izquierdo, L. Nagy, Á. Varga, J. J. Santana, G. Nagy and R. M. Souto, *Electrochim. Acta*, 2011, **56**, 8846.

31. B. M. Fernández-Pérez, J. Izquierdo, S. González, and R. M. Souto, *J. Solid State Electrochim.*, 2014, **18**, 2983.

32. Y. Konishi, Y. Nakamura Y. Fukunaka, K. Tsukada and K. Hanasaki, *Electrochim. Acta*, 2003, **48**, 2615.

33. M. Ota, S. Izuo, K. Nishikawa, Y. Fukunaka, E. Kusaka, R. Ishii and J.R. Selman, *J.Electroanal. Chem.* 2003, **559**, 175.

34. E. M. Sherif, R. M. Erasmus, J. D. Comins, *Electrochim. Acta*, 2010, **55**, 3657.

35. T. Yamanaka, H. Nakagawa, S. Tsubouchi, Y. Domi, T. Doi, T. Abe and Z. Ogumi, *J. Electrochem. Soc.*, 2017, **164**, A2355.

36. H. Hirayama, N. Tachikawa, K. Yoshii, M. Watanabe and Y. Katayama, *Electrochemistry*, 2015, **83**, 824.

37. K. Nishikawa, Y. Fukunaka, E. Chassaing and M. Rosso, *Electrochim. Acta*, 2013, **100**, 342.

38. E. Chassaing, M. Rosso, K. Nishikawa, Y. Fukunaka, *Int. J. Microgravity Sci. Appl.*, 2008, **25**, 507

39. M. Herstedt, M. Smirnov, P. Johansson, M. Chami, J. Grondin, L. Servant, J. C. Lassègues, *J. Raman Spectrosc.*, 2005, **36**, 762.

40. C. Zhang, K. Ueno, A. Yamazaki, K. Yoshida, H. Moon, T. Mandai, Y. Umebayashi, K. Dokko and M. Watanabe, *J. Phys. Chem. B*, 2014, **118**, 5144.

41. D. Brouillette, D. E. Irish, N. J. Taylor, G. Perron, M. Odziemkowski and J. E. Desnoyers, *Phys. Chem. Chem. Phys.*, 2002, **4**, 6063.

42. S. Tsuzuki, T. Mandai, S. Suzuki, W. Shinoda, T. Nakamura, T. Morishita, K. Ueno, S. Seki, Y. Umebayashi, K. Dokko and M. Watanabe, *Phys. Chem. Chem. Phys.*, 2017, **19,** 18262.

43. R. J. Blint, *J. Electrochem. Soc.*, 1995, **142**, 696.

44. L. Aguilera, S. Xiong, J. Scheers and A. Matic, *Journal of Molecular Liquids*, 2015, **210**, 238.

45. H. Moon, R. Tatara, T. Mandai, K. Ueno, K. Yoshida, N. Tachikawa, T. Yasuda, K. Dokko and M. Watanabe, *J. Phys. Chem.*, 1996, **100**, 3089.

46. D. Aurbach and A. Zaban, *J. Electroanal. Chem.*, 1993, **348**, 155.

47. D. Aurbach and A. Zaban, *J. Electroanal. Chem.*, 1994, **367**, 15.

48. A. Zaban, E. Zinigrad and D. Aurbach, *J. Phys. Chem.*, 1996, **100**, 3089.

49. K. Nishikawa, K.Shinoda, *J. Phys. Chem. Lett.*, 2021, **12**, 3922.